Drift-kinetic simulation of neoclassical transport with impurities in tokamaks

R. A. Kolesnikov,[1] W. X. Wang,[2] F. L. Hinton,[3] G. Rewoldt,[2] and W. M. Tang[2]

[1]*Los Alamos National Laboratory, Los Alamos, New Mexico 87544, USA*
[2]*Plasma Physics Laboratory, Princeton, New Jersey 08543, USA*
[3]*University of California, San Diego, La Jolla, California 92093, USA*

Plasmas in modern tokamak experiments contain a significant fraction of impurity ions in addition to the main deuterium background ions. A new multiple ion-species δf particle simulation capability has been developed to self-consistently study the nonlocal effects of impurities on neoclassical transport in toroidal plasmas. A new algorithm for an unlike-particle collision operator, including test-particle and conserving field-particle parts, is described. Effects of the carbon impurity on the main deuterium species heat flux as well as an ambipolar radial electric field in a National Spherical Torus Experiment (NSTX) [M. Ono, S. M. Kaye, Y.-K. M. Peng *et al.*, Nucl. Fusion **40**, 557 (2000)] configuration were studied. A difference between carbon poloidal rotation found from simulation and from conventional theoretical estimates has been investigated and was identified to be a nonlocal finite orbit effect. In the case of large-aspect ratio tokamak configurations with steep toroidal flow profiles, we propose a theoretical model to describe this nonlocal effect. The dominant mechanisms captured by the model are associated with ion parallel velocity modification due to steep toroidal flow and radial electric field profiles. We present simulation results for carbon poloidal velocity in NSTX. Comparisons with neoclassical theory are discussed. © *2010 American Institute of Physics*. [doi:10.1063/1.3310839]

I. INTRODUCTION

In the present advanced tokamak experiments the improved confinement regime is achieved by reducing the turbulent transport in the ion channel. To understand the performance of such toroidal devices, the experimental data are normally compared with the irreducible neoclassical transport level. While neoclassical theory has been well developed,[1] there is a need for direct numerical solution of the drift-kinetic equations globally, from the magnetic axis to the plasma boundary, with appropriate boundary conditions. This is necessary if one needs to capture nonlocal physics near the magnetic axis or steep profile gradients where basic assumptions of most local theories are violated. Also, the large scale ambipolar electric field must be self-consistently calculated by solving the neoclassical Poisson's equation. Self-consistency of the electric field, a feature absent from neoclassical theories, is important to maintain transport ambipolarity.[2]

A generalized global particle-in-cell (PIC) neoclassical code GTC-NEO which satisfies these criteria has been developed by Wang *et al.*[3] for a single ion species plasma. Using a δf method with a shifted Maxwellian background distribution function, GTC-NEO numerically solves an initial value problem for the drift-kinetic equation with a self-consistent radial electric field. The experimental plasma profiles for temperature, density, and toroidal angular frequency together with realistic magnetohydrodynamic (MHD) equilibria from the TRANSP (Ref. 4) code are used in the code.

In addition to the main ion species, which is normally deuterium, most experimentally relevant plasmas contain one or more ion species. These additional impurity species may

be deliberately introduced into the system or may be an undesirable product of interaction between the plasma and the wall of the device. While the densities of these extra species may be small compared to the density of the main deuterium background, it is generally known[5] that the amount of the impurity contribution to the ion thermal conductivity is of order

$$\alpha_{DI} = \left(\frac{Z_I}{Z_D}\right)^2 \left(\frac{n_I}{n_D}\right), \tag{1}$$

where Z and n stand for charge number and density and subscripts D and I denote main and impurity species, respectively. For the National Spherical Torus Experiment[6] (NSTX) plasmas with a fully stripped carbon impurity, $\alpha_{DI} > 1$. Consequently, impurity particles can make a significant contribution to the main deuterium heat flux indirectly by producing additional cross-species collisions.

The GTC-NEO code has been updated to solve drift-kinetic equations for an arbitrary number of ion species. This was enabled by the development of an unlike-particle collision operator for the PIC simulation technique. In addition to a test-particle operator, a field-particle operator which conserves particle number, energy, and momentum has been developed and implemented into the GTC-NEO code. In this paper we investigate the effects of these additional impurity collisions on the main ion species thermal flux as well as on the ambipolar radial electric field in NSTX configurations.

This paper also addresses the physics of nonlocal effects associated with finite orbits on poloidal rotation[7–10] using the new global neoclassical simulations with impurities. We found that the role of nonlocal effects for the poloidal flow

may be much more pronounced than their role for the heat flux and radial electric field. In addition to mechanisms previously studied, such as the effect of large rotation,[11] finite ion orbit effects might be important to account for the difference between the poloidal rotation observed in the experiment and predicted from the neoclassical theory. Based on investigation of large-aspect ratio tokamak configurations with steep toroidal flow profiles, we further propose a theoretical model which captures the dominant mechanisms underlying the nonlocal effects found in the simulations. These mechanisms are identified to be associated with generation of extraparticle parallel velocity due to *shear in the toroidal flow* and *squeezing in the radial electric field*. We use predictions for the carbon poloidal velocity from multispecies simulations and the theoretical model to compare with neoclassical theory.

The remainder of this paper is organized as follows. In Sec. II, the simulation model is described with the details of the unlike-particle collision operator being discussed in Sec. III. The effects of the carbon impurity on the radial electric field and the deuterium heat flux have been investigated for NSTX configurations in Sec. IV. In Sec. V, we propose a model to understand the nonlocal effects observed in the simulation of the carbon poloidal velocity.

II. BASIC EQUATIONS

Using the δf algorithm,[3] we solve the following equation:

$$\left(\frac{\partial}{\partial t} + \dot{X} \cdot \frac{\partial}{\partial X}\right)\delta f_s = -\dot{X} \cdot \frac{\partial}{\partial X}F_{0s} + \sum_b \left(C_{sb}[F_{0s}, \delta f_b]\right.$$
$$\left. + C_{sb}[\delta f_s, F_{0b}]\right). \quad (2)$$

On the right hand side is the linearized collision operator $\Sigma_b C_{sb}[f_s, f_b]$, which includes self-collisions and cross collisions of ion species s. The guiding center coordinates $X = (x, \rho_\|, \mu)$ evolve according to the Lagrangian equations,[12]

$$\frac{d}{dt}\left(\frac{\partial}{\partial \dot{X}}L_s\right) - \frac{\partial}{\partial X}L_s = 0. \quad (3)$$

Here $x = (r, \theta, \zeta)$ and r, θ, and ζ are the radial, poloidal, and toroidal coordinates, respectively. $\dot{\mu} = 0$ due to conservation of the adiabatic moment. The Lagrangian is given by $L_s = Z_s e \boldsymbol{p} \cdot \dot{x}/c - H_s$, with e and c being the proton charge and speed of light, respectively. Here $\boldsymbol{p} = (p_r, p_\theta, p_\zeta)$ is the canonical angular momentum and the Hamiltonian is

$$H_s = \frac{Z_s^2 e^2}{2m_s c^2}\rho_\|^2 B^2 + \mu B + Z_s e \Phi, \quad (4)$$

where the magnetic moment $\mu = m_s v_\perp^2/2B$ and the parallel gyroradius $\rho_\| = m_s v_\|/Z_s e B$ are expressed in terms of the parallel and perpendicular velocities $v_\|$ and $v_\perp$. $\Phi(r)$ is the electric potential. The spatial part of $\dot{x}$ may be rewritten in more conventional form as $\boldsymbol{v}_\| + \boldsymbol{v}_d$, where the guiding center velocity $\boldsymbol{v}_d$ includes both the $-\nabla\Phi \times \boldsymbol{B}$ drift and the ∇B drift in an inhomogeneous magnetic field.

The time-independent local shifted Maxwellian distribution function F_{0s} satisfies

$$C_{sb}[F_{0s}, F_{0b}] = 0, \quad (5)$$

and is expressed in the following form:[3]

$$F_{0s} \equiv F_{0s}(n_s, T, U_\|)$$
$$= n_s\left(\frac{m_s}{2\pi T}\right)^{3/2}\exp\left[-\frac{m_s}{T}((v_\| - U_\|)^2/2 + \mu B)\right]. \quad (6)$$

Here $n_s(r) \equiv \langle n_s(r, \theta)\rangle$, $T(r)$, and $\omega_\zeta(r)$ are experimentally given profiles for the ion density, temperature, and toroidal angular frequency. Parallel velocity and toroidal angular frequency are related according to $\omega_\zeta(r) = [B/I(r)]U_\|(r) + [B^2/I(r)n_s(r)]K(r)$, where $K(r) = 0$, since the only zeroth-order flow velocity allowed is a locally rigid toroidal rotation.[13] Here $I(r) = RB_\zeta$, with R being the major radius. These quantities together with $\Phi(t=0)$ serve as initial conditions for our simulation. $\boldsymbol{B}_\zeta = I\nabla\zeta$ and $\boldsymbol{B}_\theta = \nabla\psi \times \nabla\zeta$ are the toroidal and poloidal components of the magnetic field $\boldsymbol{B}$, where $2\pi\psi$ stands for the poloidal magnetic flux.

Note that we choose to have the same ion temperature $T(r)$ and parallel flow $U_\|(r)$ profiles in the distribution functions (6) for all ion species. This is to make sure that Eq. (5) is satisfied. However, these quantities might be different for different species; the difference is captured by the initial $\delta f_s(t=0)$ as follows:

$$\delta f_s(t=0) = F_{0s}(n_s, T_s, U_{\|s}) - F_{0s}(n_s, T, U_\|), \quad (7)$$

where $T_s(r)$ and $U_{\|s}(r)$ are experimentally given profiles for species s.

The self-consistent ambipolar potential $\Phi(r)$ in general geometry is included via the following (neoclassical Poisson's) equation:[2]

$$\left(\langle|\nabla r|^2\rangle + 4\pi c^2\sum_s n_s m_s\left\langle\frac{|\nabla r|^2}{B^2}\right\rangle\right)\frac{\partial^2\Phi}{\partial t\,\partial r} = 4\pi\sum_s Z_s e \Gamma_s, \quad (8)$$

which is obtained from Poisson's and the continuity equations. Angular brackets denote a flux surface average. The second term on the left hand side is the classical polarization current summed over species. On the right hand side, $Z_s e \Gamma_s$ is the radial ion guiding center current of species s, with the particle flux being defined by the following expression:

$$\Gamma_s \equiv \left\langle\int d^3v(\boldsymbol{v}_d \cdot \nabla r)\delta f_s\right\rangle. \quad (9)$$

Our algorithm uses a two-weight approach.[14] Defining the marker distribution function for species s in the extended phase space

$$g_s(X, w, p, t) \sim \sum_i \delta[X - X_{si}(t)]\delta[w - w_{si}(t)]\delta[p - p_{si}(t)], \quad (10)$$

the equations for the marker particle weights w and p satisfy

$$\int dw dp w g_s = \delta f_s, \tag{11}$$

$$\int dw dp (1-p) g_s = F_{0s}. \tag{12}$$

III. UNLIKE-SPECIES COLLISION OPERATOR

The linearized unlike-particle collision operator for species a colliding with species b is written as

$$C_{ab}[F_{0a}, \delta f_b] + C_{ab}[\delta f_a, F_{0b}] = C_{ab}^{\mathrm{TP}}(\delta f_a) + C_{ab}^{\mathrm{FP}}(\delta f_b). \tag{13}$$

The first term on the right hand side is the test-particle operator to describe the drag and diffusion part of the collisions. The standard Monte Carlo technique[15] is utilized in the drift-kinetic simulation to implement this operator.

The second term on the right hand side in Eq. (13) is the field-particle operator. This operator appears as a source term in Eq. (2), and not being sensitive to the details of δf_b, may be rewritten in the following form:

$$C_{ab}^{\mathrm{FP}}(\delta f_b) = \sum_{k=0}^{N-1} C_{abk}^{\mathrm{FP}}(\delta f_b), \tag{14}$$

$$C_{abk}^{\mathrm{FP}}(\delta f_b) = (\mathcal{H}_{ab}(v) \delta N_{ab}^k + \mathcal{R}_{ab}(v) v_{\parallel} \delta P_{ab}^k + \mathcal{Q}_{ab}(v) \delta E_{ab}^k).$$

The functions $\mathcal{H}_{ab}$, $\mathcal{R}_{ab}$, and $\mathcal{Q}_{ab}$ are to be determined. Operator (14) is implemented as a sequence of N iterations to enforce the appropriate conservation constraints. Specifically, at initial $k=0$ iteration, the particle number, momentum, and energy gained by species a field particles must equal that lost by species b test particles,

$$\delta N_{ab}^0 = 0, \tag{15}$$

$$\delta P_{ab}^0 = -\int d^3v \, m_b v_{\parallel} C_{ba}^{\mathrm{TP}}(\delta f_b), \tag{16}$$

$$\delta E_{ab}^0 = -\int d^3v \, (m_b v^2/2) C_{ba}^{\mathrm{TP}}(\delta f_b). \tag{17}$$

Since a finite number of simulation markers are used, the consequent iterations are necessary to further improve the conservation properties according to

$$\delta N_{ab}^n = \int d^3v \, C_{abn-1}^{\mathrm{FP}}(\delta f_b), \tag{18}$$

$$\delta P_{ab}^n = \int d^3v \, m_b v_{\parallel} C_{abn-1}^{\mathrm{FP}}(\delta f_b), \tag{19}$$

$$\delta E_{ab}^n = \int d^3v \, (m_b v^2/2) C_{abn-1}^{\mathrm{FP}}(\delta f_b). \tag{20}$$

An additional constraint comes from the requirement that the linearized operator must have the correct null space, that is

$$C_{ab}^{\mathrm{TP}}(\delta f_a) + C_{ab}^{\mathrm{FP}}(\delta f_b) = 0, \tag{21}$$

when δf_a and δf_b are perturbations of Maxwellians with the same parallel flow velocity and the same temperature perturbation,

$$C_{ab}^{\mathrm{TP}}(m_a v_{\parallel} F_{0a}) + C_{ab}^{\mathrm{FP}}(m_b v_{\parallel} F_{0b}) = 0, \tag{22}$$

$$C_{ab}^{\mathrm{TP}}(m_a v^2 F_{0a}) + C_{ab}^{\mathrm{FP}}(m_b v^2 F_{0b}) = 0. \tag{23}$$

With appropriate choices of multiplying factors, the functions $\mathcal{R}_{ab}$ and $\mathcal{Q}_{ab}$ may be found as follows:

$$\mathcal{R}_{ab}(v) v_{\parallel} F_{0a} = \frac{C_{ab}^{\mathrm{TP}}(m_a v_{\parallel} F_{0a})}{\int d^3v \, m_a v_{\parallel} C_{ab}^{\mathrm{TP}}(m_a v_{\parallel} F_{0a})}, \tag{24}$$

$$\mathcal{Q}_{ab}(v) F_{0a} = \frac{C_{ab}^{\mathrm{TP}}(m_a v^2 F_{0a})}{\int d^3v \, (m_a v^2/2) C_{ab}^{\mathrm{TP}}(m_a v^2 F_{0a})}. \tag{25}$$

Since we use Maxwellian background distribution functions, these expressions may be simplified by analytically computing the Rosenbluth potentials,[15]

$$\mathcal{R}_{ab}(v) = \frac{3\sqrt{\pi}}{4 n_a T}(1 + m_b/m_a)^{3/2} y_b^{-3/2} \phi(y_b), \tag{26}$$

$$\mathcal{Q}_{ab}(v) = \frac{\sqrt{\pi}}{2 n_a T}(1 + m_b/m_a)^{3/2} y_b^{-1/2}(m_a/m_b - d/dy_b)\phi(y_b), \tag{27}$$

where $\phi(y) = 2/\sqrt{\pi} \int_0^y e^t \sqrt{t} \, dt$ and

$$y_b = v^2/v_b^2 = m_b v^2/(2T). \tag{28}$$

While the test-particle operator theoretically conserves the particle number, the numerical implementation of only the first term C_{ab0}^{FP} in the field-particle operator (14) would lead to unsatisfactory conservation of particle number.[14] Thus the simultaneous enforcement of conservation of all three quantities according to Eq. (14) is required. While the choice of the $\mathcal{H}_{ab}$ function is not unique, we take

$$\mathcal{H}_{ab}(v) = 1 - \mathcal{Q}_{ab}(v), \tag{29}$$

which satisfies both Eqs. (18)–(20) and Eqs. (22) and (23).

The equations for the two marker weights become

$$\dot{w} = \frac{1-p}{F_{0s}}\left(-\frac{DF_{0s}}{Dt} + \sum_b C_{sb}^{\mathrm{FP}}(\delta f_b)\right) - \eta(w - \bar{w}_s), \tag{30}$$

$$\dot{p} = \frac{1-p}{F_{0s}}\left(-\frac{DF_{0s}}{Dt}\right) - \eta(p - \bar{p}_s). \tag{31}$$

Here η is the damping rate.[16] The fields $\bar{w}_s$ and $\bar{p}_s$ are computed in such a way as to ensure that the first three moments of δf_s are preserved through this weight spread reduction scheme.

In Fig. 1(a), we show the time evolution of the radial electric field $E_r = -\partial\Phi/\partial r$ (at $r/a = 0.45$) as it approaches a steady state. The time is normalized to deuterium-deuterium collision frequency ν_{DD}, where $\nu_{ab} = 4\pi n_b Z_a^2 \times Z_b^2 e^4 \ln \Lambda_{ab}/m_a^2 v_{tha}^3$. In Fig. 1(b), the corresponding evolution of $Z_s \Gamma_s$ is illustrated for both deuterium and carbon. We
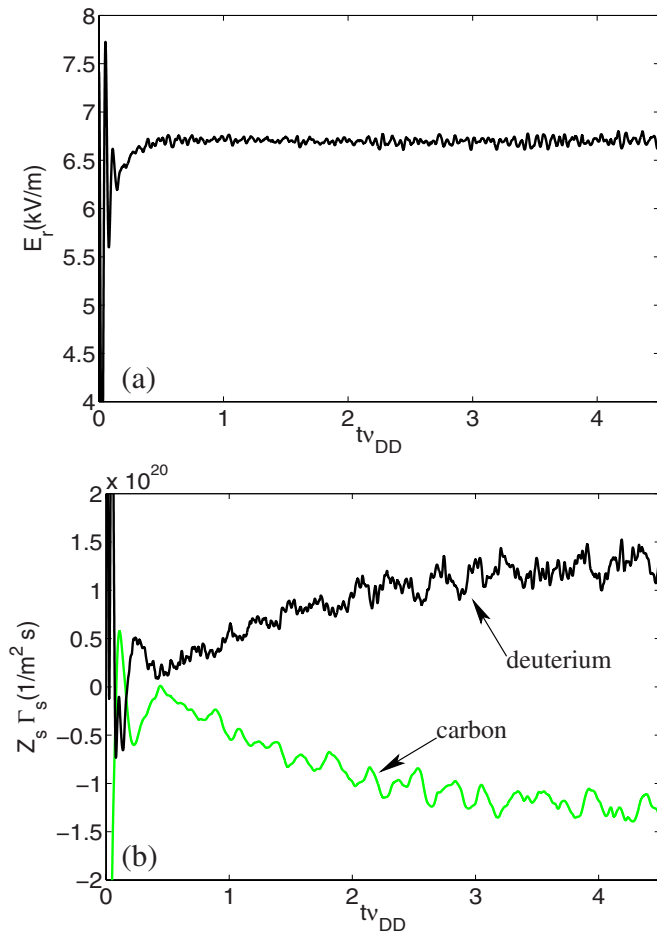
FIG. 1. (Color online) (a) Time dependence of the radial electric field (at $r/a=0.45$) for NSTX shot #129 059 at $t=0.695$ s. (b) Time dependences of $Z_s\Gamma_s$ for deuterium and carbon.

FIG. 2. (Color online) Temperature (a) and density (b) profiles for NSTX shot #112989a09 at $t=0.190$ s.

have verified that the ambipolar radial electric field reaches steady state when the total radial guiding center current [the right hand side of Eq. (8)] vanishes,

$$\sum_s Z_s e \Gamma_s = 0, \tag{32}$$

while individual particle fluxes Γ_s stay finite.

IV. EFFECT OF CARBON IMPURITY ON HEAT FLUX AND RADIAL ELECTRIC FIELD

Here we report simulation results for E_r and the heat flux in NSTX experiment with bulk deuterium and impurity carbon ions. In experiments, the radial force balance relation,

$$E_r = \frac{1}{Z_s e n_s} \frac{\partial n_s T_s}{\partial r} + \frac{1}{c}(B_\theta U_\zeta - B_\zeta U_\theta), \tag{33}$$

is utilized to determine E_r. This balance holds separately for bulk and impurity ion species. However, since most of the measurements are available only for impurities, the radial force balance for impurities is used to deduce E_r from measured $n_s(r)$, $T_s(r)$, and $U_\zeta(r)$ profiles. The poloidal flow $U_\theta(r)$ profile is usually replaced by the local neoclassical expression (38).
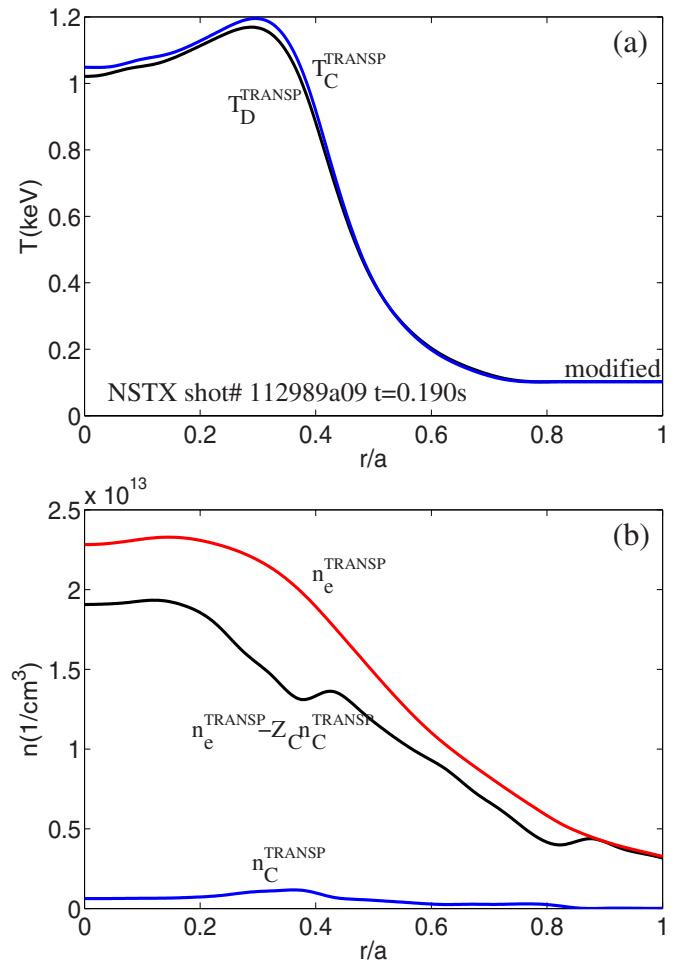
Our global neoclassical simulations with the GTC-NEO

code solve drift-kinetic equations for the ion species self-consistently with the neoclassical Poisson's equation. This simulation calculates the equilibrium radial electric field and the heat flux keeping all nonlocal effects based on first principles. Figure 2 shows some of the densities and temperatures supplied by the TRANSP code for a NSTX L-mode discharge with an internal transport barrier (ITB). In general, the TRANSP code supplies profiles, including density profiles, for various ion species n_I^{TRANSP} as well as electrons n_e^{TRANSP}, with quasineutrality condition being satisfied according to $n_e^{TRANSP}=\Sigma_I Z_I n_I^{TRANSP}$.

In Fig. 3, a simulation with a single, deuterium, species (black curve) predicts a deeper E_r well compared to the E_r profile inferred from the carbon radial force balance (red dashed curve) with the neoclassical poloidal flow. This result was obtained in Ref. 3 by assuming that all ion species (supplied by the TRANSP code) are deuterium [the deuterium density n_D in GTC-NEO input was taken to be equal to n_e^{TRANSP}, according to Fig. 2(b)].

With new multiple-species capability, we investigate the effect of impurity carbon ions on E_r, particularly on the deep well discovered in single-species simulation. This involves adding carbon $n_C=n_C^{TRANSP}$ as well as removing a fraction of deuterium $Z_C n_C$ (to formally satisfy quasineutrality condition) to the simulation. We do it in two steps. First, we
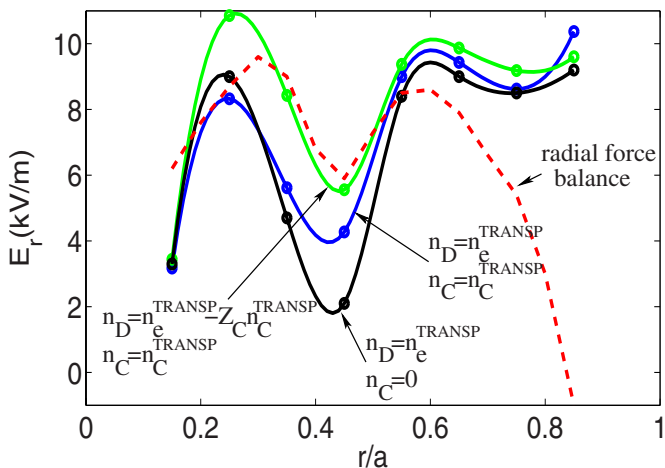
FIG. 3. (Color online) Simulated radial electric field for NSTX shot #112989a09 at $t=0.190$ s, compared with E_r calculated from the carbon radial force balance.

only add carbon, and the simulation with $n_D=n_e^{TRANSP}$ and $n_C=n_C^{TRANSP}$ results in the dark grey (blue) curve; the presence of the impurity species reduces the depth of the well. Second, for a fixed carbon density $n_C=n_C^{TRANSP}$, we decrease deuterium density in the simulation down to $n_D=n_e^{TRANSP}-Z_C n_C$; this further reduces the depth of the well [light grey (green) curve], bringing the E_r profile to even better agreement with the estimate from the radial force balance. From this observation we conclude that including a carbon impurity in the simulation may be important for calculation of E_r near an ITB; it further brings E_r to better agreement with the estimate from the radial balance relation, which implies that finite orbit effects on E_r are weak.

In Fig. 4, we examine the heat flux for the same NSTX discharge with an ITB. Due to the reversed local ∇T near the magnetic axis [Fig. 2(a)], the local transport theory [dashed red curve from the NCLASS (Ref. 17) code] predicts an inward deuterium heat flux in this region. Due to the nonlocal effects associated with finite ion orbits, both single-species and two-species simulations (grey curves) predict outward
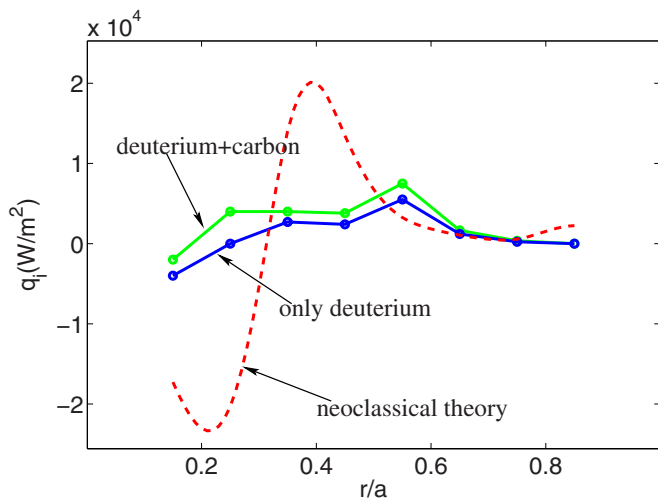

FIG. 4. (Color online) Simulated deuterium heat flux vs r/a for NSTX shot #112989a09 at $t=0.190$ s.
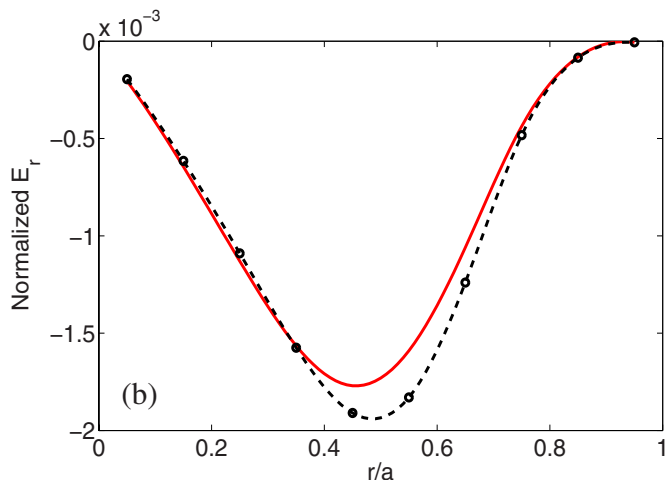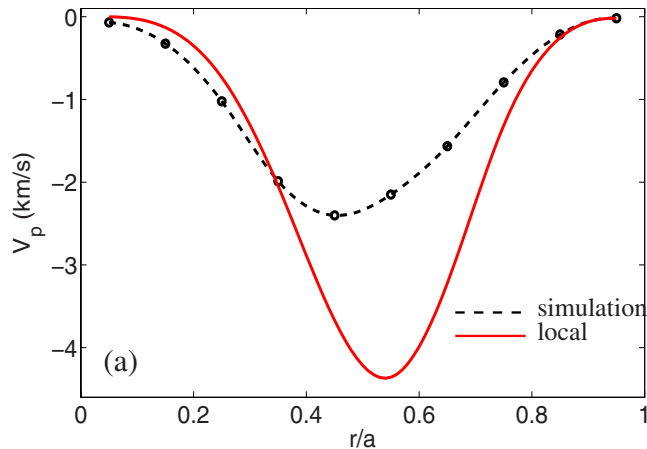

FIG. 5. (Color online) (a) The deuterium poloidal velocity vs normalized minor radius from simulation and local neoclassical prediction. (b) The radial electric field obtained from simulation and radial force balance.

heat fluxes. Finite orbit effects in the simulation also tend to produce extra smoothing in the heat flux profile. Addition of carbon increases the deuterium heat flux by a factor which may be roughly estimated as $(1+\alpha_{DC})$ from Eq. (1).

V. POLOIDAL VELOCITY WITH FINITE ORBIT EFFECT

One of the findings of our systematic simulations is the indication that the physics associated with particle finite orbits plays an important role in poloidal flow. Figure 5(a) shows the simulation result for the deuterium poloidal velocity U_θ (the dashed black curve) in a one-species large-aspect ratio system (major over minor radius, $R/a=10$) with circular magnetic surfaces in the presence of large shear in the toroidal velocity. The equilibrium magnetic field and major radius are $B=3T$ and $R=5m$. The ratios of the thermal banana orbit widths over typical density $n(r)$, temperature $T(r)$ and toroidal rotation frequency $\omega(r)$ scale lengths are $\Delta_b/L_n \sim \Delta_b/L_T \sim 0.3$ and $\Delta_b/L_\omega \sim 0.5$ at $r/a \sim 0.5$, respectively.

The grey (red) curve in Fig. 5(a) is an estimate from the local neoclassical theory, which tends to overestimate the amplitude of the poloidal rotation by $\sim 50\%$ at $r/a \sim 0.55$. Figure 5(b) shows the self-consistent neoclassical radial electric field E_r from the simulation and from local theory. The

difference between the two curves in both panels is due to finite orbit effects. This has been verified by increasing the collision frequency and observing that the difference gradually vanishes; enhanced collisions destroy the large particle orbits responsible for nonlocal effects. As illustrated by Fig. 5, while these nonlocal effects do not significantly modify the electric field ($\sim 10\%$ at $r/a \sim 0.55$), they are certainly important for the poloidal flow.

An expression for the poloidal velocity U_θ is obtained by constructing an appropriate combination of parallel $U_\parallel$ and perpendicular $U_\perp$ velocities,

$$U_\theta = U_\parallel \frac{B_\theta}{B} + U_\perp \cdot \frac{B_\theta}{B_\theta}. \tag{34}$$

The sign conventions for U_θ and U_ζ are $U_\theta \cdot U_{\text{dia}}^e > 0$ and $U_\zeta \cdot U_{\text{dia}}^i > 0$. Here $U_{\text{dia}}^e = -(c/neB)\hat{b} \times \partial nT/\partial r$ and $U_{\text{dia}}^i = -U_{\text{dia}}^e/Z$ are electron and ion diamagnetic velocities. While $U_\perp$ captures the drift perpendicular to the magnetic field

$$U_\perp = \frac{c}{nZeB}\hat{b} \times \left(\frac{\partial nT}{\partial r} - ZenE_r\right), \tag{35}$$

the $U_\parallel$ can be evaluated as a sum of a local neoclassical estimate and some unknown nonlocal correction $\Delta \mathcal{U}_\parallel$,

$$U_\parallel = U_{\parallel 0} + \Delta \mathcal{U}_\parallel = \frac{cIT}{ZeB\psi'}\left(-\frac{\partial \ln nT^{(1-k)}}{\partial r} + \frac{Ze}{T}E_r\right) + \Delta \mathcal{U}_\parallel. \tag{36}$$

Here $\psi' = \partial \psi/\partial r$, and k is a collisionality dependent parameter. Note that here we neglect possible nonlocal effects on $U_\perp$, such as orbit shrinking due to distorted gyro-orbits.[18] These effects are not captured by our GTC-NEO drift-kinetic simulation as well as analytical calculation in this section.

Substitution of Eqs. (35) and (36) into Eq. (34) gives

$$U_\theta = U_{\theta 0} + \frac{B_\theta}{B}\Delta \mathcal{U}_\parallel, \tag{37}$$

where most of the terms cancel resulting in

$$U_{\theta 0} = \frac{B_\theta}{B}k\frac{Ic}{ZeB\psi'}\frac{\partial T}{\partial r}. \tag{38}$$

As a consequence, the standard neoclassical part of the poloidal flow $U_{\theta 0}$ only depends on the radial temperature gradient.

In a self-consistent momentum-conserving simulation, for a given set of $n(r)$, $T(r)$, and $\omega_\zeta(r)$ profiles, the radial electric field E_r evolves to satisfy Eq. (36). Also while the correction from the nonlocal $\Delta \mathcal{U}_\parallel$ to E_r might be small, its effect on the poloidal flow U_θ, due to a cancellation in Eq. (37), might be significant, especially in the case of strong ω_ζ.

One of the important findings is that for a given set of radial profiles and magnetic field configuration, using an assumption of uniform temperature ($\partial T/\partial r = 0$), the finite orbit effect on the parallel flow $\Delta \mathcal{U}_{\parallel 1}$ may be calculated. To understand the nonlocal effects in a collisionless system, we construct a quasiequilibrium function of constants of the particle motion and at the same time make it as close to a shifted

Maxwellian as possible. The velocity moment of such a function will give an expression for the nonlocal effect. While uniform temperature assumption is used in the calculation, we will apply the resulting expression to systems with nonuniform temperature profiles.

The distribution function $f(\boldsymbol{x}, \epsilon, \mu)$,

$$f = (m/2\pi T)^{3/2}N(\psi^\star)\exp(-a\epsilon - b\mu), \tag{39}$$

is a function of the guiding center canonical angular momentum $\psi^\star = \psi - Iv_\parallel/\Omega$, the total energy $\epsilon = (v_\parallel^2 + v_\perp^2)/2 + Ze\Phi(\psi)/m$, and the magnetic moment $\mu = v_\perp^2/2B$. The constants a and b are to be determined.

By substituting $N(\psi^\star) = N_0\exp(-\beta\psi^\star - \gamma\psi^{\star 2})$ into Eq. (39) and equating the magnetic surface average of the coefficients in front of $v_\parallel^2$ and $v_\perp^2$, we obtain

$$f = \left(\frac{m}{2\pi T}\right)^{3/2}N_0\exp\left(-\beta\psi - \gamma\psi^2 - a\frac{Ze\Phi}{m} + \frac{m}{2T}U_\parallel^2\right)$$
$$\times\exp\left(-\frac{m}{2T}[(v_\parallel - U_\parallel)^2 + v_\perp^2]\right). \tag{40}$$

Here the temperature and the parallel flow are defined to be

$$\frac{m}{T} = a + \frac{2\gamma I^2 m^2 c^2}{Z^2 e^2}\langle B^{-2}\rangle, \tag{41}$$

$$U_\parallel = \frac{cTI}{ZeB}(\beta + 2\gamma\psi), \tag{42}$$

with $\langle \ \rangle$ being a magnetic surface average.

Taking the density moment of Eq. (40) and using Eqs. (41) and (42) along with $\gamma = (Ze/2cT)\partial\omega/\partial\psi$, we obtain $U_\parallel = U_{\parallel 0} + \Delta \mathcal{U}_{\parallel 1}$, where $U_{\parallel 0}$ is the local prediction given by Eq. (36) with $\partial T/\partial r = 0$. The nonlocal contribution is calculated to be

$$\Delta \mathcal{U}_{\parallel 1} = -\frac{ZeI}{m^2 c\Omega}\left\langle\frac{I^2}{\Omega^2}\right\rangle T\frac{\partial \ln nT}{\partial\psi}\frac{\partial\omega}{\partial\psi}. \tag{43}$$

$\Omega = ZeB/mc$ is the cyclotron frequency.

The mechanism underlying the nonlocal effect given by Eq. (43) is generation of extraparallel velocity near steep toroidal flow gradients. This implies that extra-poloidal velocity is also produced trivially via the relation $\Delta \mathcal{U}_{\theta 1} = (B_\theta/B)\Delta \mathcal{U}_{\parallel 1}$. In Fig. 7, $\Delta \mathcal{U}_{\theta 1}$ is shown by the dashed green curve.

It has been verified that for a system with uniform temperature ($U_{\theta 0} = 0$), the simulation result for the poloidal flow quantitatively agrees with Eq. (43). To understand the validity of Eq. (43) in the case of nonuniform temperature, in Fig. 6(a), along with the simulation result and the local formula $U_{\theta 0}$, we plot $U_{\theta 0} + \Delta \mathcal{U}_{\theta 1}$ (dashed green curve). It is clear that while the local formula overestimates the amplitude of the poloidal flow, addition of the orbit shearing nonlocal term leads to better agreement with the simulation result. Comparing the dashed black and dashed green curves, we observe that they cross near $\partial E_r/\partial r = 0$ [see Figs. 6(a) and 6(b)]. We conclude that another important nonlocal effect should be proportional to $\partial E_r/\partial r$.
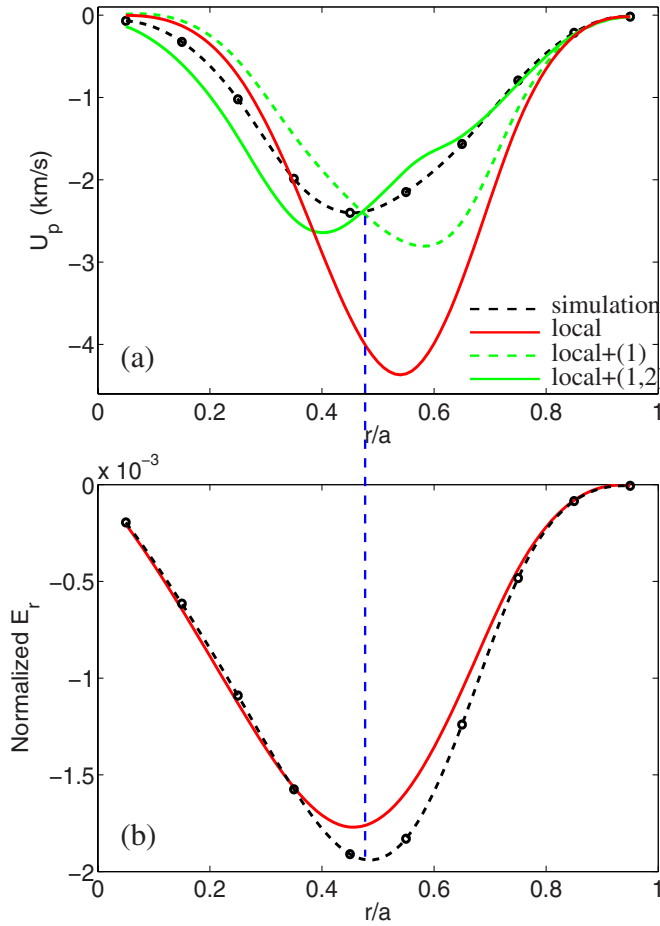
FIG. 6. (Color online) (a) The deuterium poloidal velocity vs normalized minor radius. Compared to Fig. 5(a), the new dashed curve is the local prediction modified by orbit shearing effect. The new solid curve also includes orbit squeezing effect. (b) The radial electric field obtained from simulation and radial force balance.

To evaluate this ion orbit squeezing effect due to the shear of the radial electric field, we again utilize a quasiequilibrium function of constants of the particle motion. We start with the following expression:

$$f = \exp(\alpha(\psi^\star) - \beta(\psi^\star)\epsilon). \tag{44}$$

Then the functions $\alpha(\psi^\star)$ and $\beta(\psi^\star)$ can be identified from the requirement that f must reduce to a shifted Maxwellian,

$$f_{sm} = n(\psi)\left(\frac{m}{2\pi T(\psi)}\right)^{3/2}$$
$$\times \exp\left(-\frac{m}{2T(\psi)}[(v_\parallel - U_\parallel(\psi))^2 + v_\perp^2]\right), \tag{45}$$

in the limit of zero orbit width, $\psi^\star - \psi \to 0$. This gives

$$\alpha(\psi) = \ln\left(\frac{m}{2\pi T(\psi)}\right)^{3/2} + \frac{Ze\Phi(\psi)}{T(\psi)}\ln n(\psi), \tag{46}$$

$$\beta(\psi) = \frac{m}{T(\psi)}. \tag{47}$$

The parallel flow will be determined by maximizing an entropy expression defined by
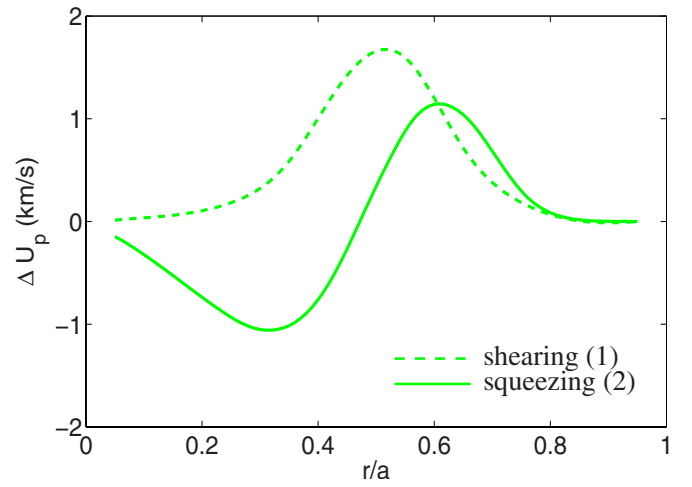

FIG. 7. (Color online) Corrections to deuterium poloidal velocity due to orbit shearing (dashed curve) and orbit squeezing (solid curve) nonlocal effects.

$$S = \frac{1}{n(\psi)}\int d^3 \boldsymbol{v} f_{sm}(\ln f - \ln f_{sm}), \tag{48}$$

where according to the small width approximation

$$\ln f - \ln f_{sm} = \alpha(\psi^\star) - \alpha(\psi) - [\beta(\psi^\star) - \beta(\psi)]\epsilon + \beta(\psi)$$
$$\times (-v_\parallel U_\parallel + U_\parallel^2/2). \tag{49}$$

The equation $\partial S/\partial U_\parallel = 0$ gives a nonlocal correction to $U_{\parallel 0}$. The term proportional to $\partial E_r/\partial r$ is

$$\Delta \mathcal{U}_{\parallel 2} = -\frac{ZeI^3}{m^2\Omega^3}T\frac{\partial \ln nT}{\partial \psi}\frac{\partial^2 \Phi}{\partial \psi^2}. \tag{50}$$

As a result of ion orbit squeezing by the electric field, an extraparallel velocity $\Delta \mathcal{U}_{\parallel 2}$ and thus extrapoloidal velocity $\Delta \mathcal{U}_{\theta 2} = (B_\theta/B)\Delta \mathcal{U}_{\parallel 2}$ are generated. In Fig. 7, $\Delta \mathcal{U}_{\theta 2}$ is shown by the solid green curve. The effect due to orbit squeezing was investigated before,[19] yielding the same result in the $\psi^\star - \psi \to 0$ limit.

In Fig. 6(a), the light grey (solid green) curve is obtained by adding both orbit shearing and orbit squeezing effects to the local estimate, $U_{\theta 0} + \Delta \mathcal{U}_{\theta 1} + \Delta \mathcal{U}_{\theta 2}$. Taking both nonlocal effects into account appears to give much better agreement with the simulation result. Note, that while GTC-NEO code is suitable for simulation of arbitrary aspect ratio systems, proposed nonlocal effects Eqs. (43) and (50) were derived with large aspect ratio assumption. Specifically, small variation of the magnetic field strength was assumed in order to justify application of surface averaging in Eq. (40); also, small orbit width approximation was used in Eq. (50).

VI. CARBON POLOIDAL VELOCITY IN NSTX

Figure 8 shows carbon poloidal velocity U_θ^C and the radial electric field versus minor radius for NSTX shot #129 059 at $t = 0.695$ s in a deuterium plasma with a carbon impurity. In the upper and lower panels, the dark grey (red) curves are obtained from the NCLASS code and radial force balance (33), respectively.
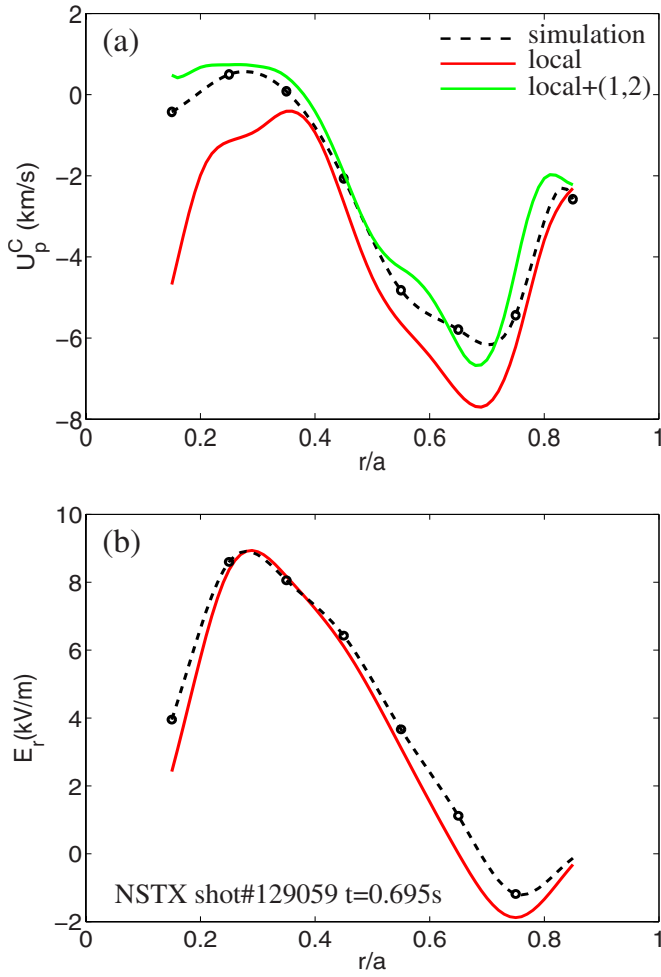
FIG. 8. (Color online) (a) The carbon poloidal velocity vs normalized minor radius. The dashed black curve is the simulation result. (b) The radial electric field obtained from the simulation and the radial force balance.

To investigate the role of the two nonlocal effects identified earlier, we carried out numerical simulations with the GTC-NEO code in the presence of both deuterium and carbon ion species. While experimental temperature and density profiles are supplied by the TRANSP code, the same (mass-averaged) toroidal velocity profiles are assumed for both ion species. This is the first fully drift-kinetic neoclassical simulation study of impurity poloidal rotation using realistic parameters for NSTX. The simulation result is given by the dashed black curves.

In order to understand the nonlocal effects, in general, one needs to consider the following system of four equations[20] for the poloidal velocity U_θ^s and the poloidal heat flux Q_θ^s for species $s = C, D$,

$$\begin{pmatrix} \hat{\mu}_1^s & \hat{\mu}_2^s \\ \hat{\mu}_2^s & \hat{\mu}_3^s \end{pmatrix} \begin{pmatrix} U_\theta^s - B_\theta/B \Delta\mathcal{U}_\parallel^s \\ Q_\theta^s \end{pmatrix}$$
$$= \sum_{b=C,D} \begin{pmatrix} l_{11}^{sb} & -l_{12}^{sb} \\ -l_{12}^{sb} & l_{22}^{sb} \end{pmatrix} \begin{pmatrix} \tilde{U}^b - B_\theta/B \Delta\mathcal{U}_\parallel^b \\ \tilde{Q}^b \end{pmatrix}. \quad (51)$$

The superscripts "C" and "D" stand for carbon and deuterium, respectively. Here, $\tilde{U}^s = V_{1s} B / \langle B^2 \rangle + U_\theta^s$ and $\tilde{Q}^s = V_{2s} B / \langle B^2 \rangle + Q_\theta^s$, where possible nonlocal effects in Q_θ^s were neglected. The neoclassical parallel viscosities $\hat{\mu}^s$ and coefficients l^{sb} as well as V_{1s} and V_{2s} are defined in Ref. 20. It is clear from Eq. (51) that the carbon poloidal velocity U_θ^s will be affected by the nonlocal effects from both the carbon $\Delta\mathcal{U}_\parallel^C$ and deuterium $\Delta\mathcal{U}_\parallel^D$ species.

To simplify the analysis, we notice that the finite orbit effect on the radial electric field primarily comes from the dominant deuterium ions. Then rewriting the radial force balance for carbon yields

$$\Delta\mathcal{U}_\theta^C \approx \frac{B_\theta}{B} \Delta\mathcal{U}_\parallel^C - \frac{B\psi'}{B_\zeta I} \Delta\mathcal{U}_\parallel^D. \quad (52)$$

Having added analytical expressions for the new nonlocal effects $\Delta\mathcal{U}_\theta^C = \Delta\mathcal{U}_{\theta1}^C + \Delta\mathcal{U}_{\theta2}^C$ together with the local formula $U_{\theta0}^C + \Delta\mathcal{U}_\theta^C$, we obtain the light grey (green) curve in Fig. 8 which agrees better with the simulation result than the local NCLASS prediction.

While the analytical theory is developed for large aspect ratio, due to the heuristic nature of our derivation, we make qualitative comparisons between analytical estimates and simulation results for NSTX to gain insight into the possible importance of the shearing and squeezing effects. For NSTX plasmas, typical features include large ion orbit size compared to the local minor radius and plasma equilibrium scale length, a large fraction of trapped particles, and large toroidal rotation with strong shear. All these features are favorable for the discussed nonlocal effects to be significant. Also, NSTX discharges usually have strong $E \times B$ shear which suppresses low-k turbulence, which not only enhances the nonlocal neoclassical effect but also minimizes the possibilities of turbulence influence on poloidal momentum transport and flow generation. As part of future plans, when a sufficient NSTX experimental database is available, statistical scans of experimental data such as $(U_\theta^{exp} - U_\theta^{local})/U_\theta^{local}$ versus $\partial\omega_\zeta/\partial\psi$ and $\partial^2\Phi/\partial\psi^2$ will provide useful information to validate the nonlocal effects discussed in this paper.

VII. CONCLUSIONS

A new multiple ion-species capability has been implemented into the global GTC-NEO PIC initial value code to self-consistently study the nonlocal effects of impurities on neoclassical transport in toroidal plasmas. A new algorithm for an unlike-particle collision operator, including test-particle and conserving field-particle parts, has been described. Using this capability, we investigated the effect of impurities on the deuterium heat flux and the radial electric field in tokamak plasmas. We verified that the nonambipolar radial electric field reaches steady state when the total radial guiding center particle current vanishes, while individual species fluxes stay finite.

Finally, we performed a neoclassical drift-kinetic simulation of poloidal velocity in a two ion-species system. New nonlocal effects due to shear in the toroidal flow and squeezing in the radial electric field are observed. A new analytical

model based on these effects has been proposed to qualitatively explain the simulation results in large aspect-ratio plasmas with steep toroidal flow profiles. The newly discovered nonlocal effects might offer insight into the role of nonlocal effects in realistic magnetic fusion devices.

ACKNOWLEDGMENTS

[1] F. L. Hinton and R. D. Hazeltine, Rev. Mod. Phys. **48**, 239 (1976).

[2] W. X. Wang, F. L. Hinton, and K. Wang, Phys. Rev. Lett. **87**, 055002 (2001).

[3] W. X. Wang, G. Rewoldt, W. M. Tang, F. L. Hinton, J. Manickam, L. E. Zakharov, R. B. White, and S. Kaye, Phys. Plasmas **13**, 082501 (2006).

[4] R. J. Goldston, in *Basic Physical Processes of Toroidal Fusion Plasmas* (Proceedings of Course and Workshop Varenna, 1985) (CEC, Brussels, 1986), Vol. 1, p. 165.

[5] S. P. Hirshman and D. J. Sigmar, Nucl. Fusion **21**, 1079 (1981).

[6] M. Ono, S. M. Kaye, Y.-K. M. Peng, G. Barnes, W. Blanchard, M. D. Carter, J. Chrzanowski, L. Dudek, R. Ewig, D. Gates, R. E. Hatcher, T. Jarboe, S. C. Jardin, D. Johnson, R. Kaita, M. Kalish, C. E. Kessel, H. W. Kugel, R. Maingi, R. Majeski, J. Manickam, B. McCormack, J. Menard, D. Mueller, B. A. Nelson, C. Neumeyer, G. Oliaro, F. Paoletti, R. Parsells, E. Perry, N. Pomphrey, S. Ramakrishnan, R. Raman, G. Rewoldt, J. Robinson, A. L. Roquemore, P. Ryan, S. Sabbagh, D. Swain, E. L. Synakowski, M. Viola, M. Williams, and J. R. Wilson, Nucl. Fusion **40**, 557 (2000).

[7] R. E. Bell, Bull. Am. Phys. Soc. **54**, 181 (2009).

[8] W. M. Solomon, K. H. Burrell, R. Andre, L. R. Baylor, R. Budny, P. Gohil, R. J. Groebner, C. T. Holcomb, W. A. Houlberg, and M. R. Wade, Phys. Plasmas **13**, 56116 (2006).

[9] K. Crombé, Y. Andrew, T. M. Biewer, E. Blanco, P. C. de Vries, C. Giroud, N. C. Hawkes, A. Meigs, T. Tala, M. von Hellermann, and K. D. Zastrow, Plasma Phys. Controlled Fusion **51**, 055005 (2009).

[10] A. R. Field, J. McCone, N. J. Conway, M. Dunstan, S. Newton, and M. Wisse, Plasma Phys. Controlled Fusion **51**, 105002 (2009).

[11] S. K. Wong, V. S. Chan, and W. M. Solomon, Phys. Plasmas **15**, 082503 (2008).

[12] R. White and L. E. Zakharov, Phys. Plasmas **10**, 573 (2003).

[13] F. L. Hinton and S. K. Wong, Phys. Fluids **28**, 3082 (1985).

[14] W. X. Wang, N. Nakajima, M. Okamoto, and S. Murakami, Plasma Phys. Controlled Fusion **41**, 1091 (1999).

[15] X. Q. Xu and M. N. Rosenbluth, Phys. Fluids B **3**, 627 (1991).

[16] S. Brunner, E. Valeo, and J. A. Krommes, Phys. Plasmas **6**, 4504 (1999).

[17] W. A. Houlberg, K. C. Shaing, S. P. Hirshman, and M. C. Zarnstorff, Phys. Plasmas **4**, 3230 (1997).

[18] K. C. Shaing, A. Y. Aydemir, and R. D. Hazeltine, Phys. Plasmas **5**, 3680 (1998).

[19] Y.-B. Kim, F. L. Hinton, H. St. John, T. S. Taylor, and D. Wroblewski, Plasma Phys. Controlled Fusion **36**, A189 (1994).

[20] P. Helander and D. J. Sigmar, *Collisional Transport in Magnetized Plasmas* (Cambridge University Press, Cambridge, 2002), p. 222.